A&A 521, A3 (2010)
DOI: 10.1051/0004-6361/201014911
© ESO 2010

Astronomy & Astrophysics

The population of planetary nebulae and H II regions in M 81

A study of radial metallicity gradients and chemical evolution*

L. Stanghellini[1], L. Magrini[2], E. Villaver[3], and D. Galli[2]

[1] National Optical Astronomy Observatories, Tucson, AZ 85719, USA
e-mail: lstanghellini@noao.edu
[2] INAF-Osservatorio Astrofisico di Arcetri, Largo E. Fermi 5, 50125 Firenze, Italy
e-mail: [laura;galli]@arcetri.astro.it
[3] Universidad Autónoma de Madrid, Departamento de Física Teórica C-XI, 28049 Madrid, Spain
e-mail: eva.villaver@uam.es

Received 1 May 2010 / Accepted 14 June 2010

ABSTRACT

Context. M 81 is an ideal laboratory to investigate the galactic chemical and dynamical evolution through the study of its young and old stellar populations.
Aims. We analyze the chemical abundances of planetary nebulae and H II regions in the M 81 disk for insight on galactic evolution, and compare it with that of other galaxies, including the Milky Way.
Methods. We acquired Hectospec/MMT spectra of 39 PNe and 20 H II regions, with 33 spectra viable for temperature and abundance analysis. Our PN observations represent the first PN spectra in M 81 ever published, while several H II region spectra have been published before, although without a direct electron temperature determination. We determine elemental abundances of helium, nitrogen, oxygen, neon, sulfur, and argon in PNe and H II regions, and determine their averages and radial gradients.
Results. The average O/H ratio of PNe compared to that of the H II regions indicates a general oxygen enrichment in M 81 in the last ~10 Gyr. The PN metallicity gradient in the disk of M 81 is $\Delta\log(\mathrm{O/H})/\Delta R_{\mathrm{G}} = -0.055 \pm 0.02$ dex/kpc. Neon and sulfur in PNe have a radial distribution similar to that of oxygen, with similar gradient slopes. If we combine our H II sample with the one in the literature we find a possible mild evolution of the gradient slope, with results consistent with gradient steepening with time. Additional spectroscopy is needed to confirm this trend. There are no type I PNe in our M 81 sample, consistently with the observation of only the brightest bins of the PNLF, the galaxy metallicity, and the evolution of post-AGB shells.
Conclusions. Both the young and the old populations of M 81 disclose shallow but detectable negative radial metallicity gradient, which could be slightly steeper for the young population, thus not excluding a mild gradients steepening with the time since galaxy formation. During its evolution M 81 has been producing oxygen; its total oxygen enrichment exceeds that of other nearby galaxies.

Key words. ISM: abundances – H II regions – planetary nebulae: general – galaxies: abundances – galaxies: evolution – galaxies: clusters: individual: M 81

1. Introduction

The study of chemical evolution of galaxies hinges on the confrontation between sets of evolutionary chemical models and arrays of observational data. Comparison of models with reliable abundance determinations are needed to understand the framework of galaxy evolution, and to test star formation history, stellar nucleosynthesis, and the mechanisms of galaxy assembly and formation.

Galactic metallicity gradients, and especially their time evolution, are important probes of galaxy formation and evolution. Observationally, most studied galaxies display a radial metallicity gradient with a negative slope, indicative of higher metallicity toward the inner galaxy. Time variation of gradient slopes in galaxies is hard to come by, given the lack of reliable time-tagging metallicity probes. From the viewpoint of theory, different models predict opposite time evolution of the metallicity gradient, showing the sensitivity of this physical parameter to the adopted parameterization of the processes (e.g., Magrini et al. 2007). A key factor to forwarding our knowledge in this field is the acquisition of high quality spectra to obtain abundances for a variety of probes, in a wide selection of different galaxies, including our own, to cover as much as possible the parameter space of initial masses, metallicities, and galaxy type.

The planetary nebula (PN) abundances of elements that are invariant during the evolution of low- and intermediate-mass stars (the so-called α-elements) probe the environment at the epoch of the formation of the PN progenitors. Oxygen, neon, sulfur, and argon are, for the most part, manufactured in high mass stars ($M > 8\ M_{\odot}$), thus their concentration in PNe across galactic disks probe the metallicity gradient in remote epochs. The metallicity gradients of PNe, compared to gradients of young stellar populations (such as those given by H II regions) allow the study of the chemical evolution of galaxies. Galactic metallicity gradients are measured in terms of $\Delta\log(\mathrm{X/H})/\Delta R_{\mathrm{G}}$ dex kpc^{-1}, where X/H is the abundance of element X with respect to hydrogen and R_{G} is the galactocentric distance.

* Full Tables 2 and 3 are only available in electronic form at the CDS via anonymous ftp to cdsarc.u-strasbg.fr (130.79.128.5) or via
http://cdsarc.u-strasbg.fr/viz-bin/qcat?J/A+A/521/A3

Planetary nebula gradients in the Milky Way indicate that the metallicity decreases inside out by 0.01 to 0.07 dex kpc^{-1} (e.g., Maciel & Quireza 1999; Henry et al. 2004; Stanghellini et al. 2006; Perinotto & Morbidelli 2006). The most recent of these studies seem to agree that the PN metallicity gradients are rather flat, i.e., their slope is not steeper than ∼−0.02 dex kpc^{-1}, and only slightly shallower than that derived from H II regions, implying that the Galactic metallicity gradient does not vary very much within the time frame of Galactic evolution. The metallicity gradients based on Galactic PNe are hindered by the uncertainties in PN distances, by the interstellar absorption in the direction of the Galactic center, and by the paucity of PN observations in the direction of the Galactic anti-center. These factors, together with the interest of studying metallicity gradients of other spiral galaxies of different morphological types and belonging to different groups, prompt us to investigate the PN (and H II region) metallicity gradients in the M 81 disk.

M 81 is the largest member of the nearest interacting group of galaxies at a distance of 3.63 ± 0.34 Mpc (Freedman et al. 2001). Its two brightest companions, M 82 and NGC 3077, are located within a projected distance of 60 kpc. The disturbed nature of the system is evident from the observations in the 21 cm emission line of H I, showing extended tidal streams and debris between the galaxies (Gottesman & Weliachew 1975; Yun et al. 1994). The simulation of Yun (1999) explains many of these tidal features as being the result of close encounters between M 81 and each of its neighbors ∼200–300 Myr ago. The most prominent debris (e.g., Sabbi et al. 2008; Weisz et al. 2008) are considered tidal dwarf galaxies, new stellar systems that formed in gas stripped from interacting galaxies.

The α-element abundances of PNe and H II regions in M 81 have remained elusive, with the exception of 17 H II regions (Garnett & Shields 1987, GS87). With the PNe (Jacoby et al. 1989; Magrini et al. 2001) and H II regions (Lin et al. 2003) locations, and their de-projected (PA = 157° and inclination = 59°, Kong et al. 2000) galactocentric distances available we are in the position to push forward a determination of abundance gradients from PNe and H II regions in the M 81 disk. The location of M 81 within its group will allow us to study the effect of galaxy interactions and mergers in the evolution of a galaxy and of its abundance gradient.

In order to sample the M 81 disk to the necessary S/N for abundance analysis we need spectroscopy with a 6–8 m class telescope. MMT/Hectospec medium-resolution spectroscopy offers the unique opportunity to study both the PNe and the H II region populations with the same setup, during the same night, and adopting the same analysis techniques, thus avoiding most biases that commonly affect the comparison of chemical abundances in population of different ages (e.g. Fe/H from old RGB stars is difficult to compare with O/H from the present time H II regions). We present here the results from the study of a sample of bright PNe in M 81, with the goal of obtaining the metallicity and explore their gradients within the M 81 disk. Their properties as a group are discussed, and compared with those of H II regions from both our MMT observations and from the literature. The combined properties of M 81 PNe and H II regions are also compared with their homologs in other nearby galaxies and in the Milky Way.

In Sect. 2 we describe the observation and analysis techniques, and give the measured fluxes and calculated abundances. Section 3 includes the analysis of the derived abundances and the determination of the metallicity gradients, Sect. 4 presents the discussion of our results, and the conclusions are in Sect. 5.

2. The MMT observations: data reduction and analysis

2.1. Observations

We obtained the spectra of PNe and H II regions in M 81 with the MMT Hectospec fiber-fed spectrograph (Fabricant et al. 2005). The spectrograph was equipped with an Atmospheric Dispersion Corrector and it was used with a single setup: 270 mm^{-1} grating at a dispersion of 1.2 Å pixel^{-1}. The resulting total spectral coverage ranged from approximately 3600 Å to 9100 Å, thus including the basic emission-lines necessary for the determination of physical and chemical properties.

The PNe were selected among those observed with the Isaac Newton Telescope (INT) with [O III], Hα, and Stromgren Y filters (Magrini et al. 2001), which allowed us to cover the whole field of M 81, and to identify a large number of disk PNe at large galactocentric distances. An earlier survey by Jacoby et al. (1989) was limited to the M 81 bulge. It is worth noting that the INT images allow us to have accurate positions (<0.5″) and finding charts for the selected PNe and H II regions, a crucial information given the crowding of the inner and spiral arm fields of M 81.

The first target selection was performed by scaling the PN brightness in [O III] with those of M 33 PNe, whose medium-resolution spectra have been observed by us using the identical technique (Magrini et al. 2009, 2010, hereafter M09, M10). We also endeavored to have PN targets at several galactocentric distances, in order to characterize the PN metallicity gradient. The instrument deploys 300 fibers over a 1 degree diameter field of view and the fiber diameter is ∼1.5″. The projected size of M 81 on the sky is smaller than the whole field of view of MTT/Hectospec, and we took advantage of this by placing some of the fibers in the outermost periphery of M 81, where some H II regions and few PNe, both belonging to the outer disk and to the intra-group population, have been identified. In addition, since the available catalog of H II regions by Lin et al. (2003) is based on Hα photometry, our INT [O III] observations have been useful to select [O III]-bright H II regions essential for chemical abundance determination. As stated by Magrini et al. (2001), we expect the misclassification of H II regions into PNe and vice-versa to be lower than ∼3% of the whole sample.

The observations were carried out in queue mode in four runs during the months of November and December 2008. Each of the observing runs consisted of 3 to 5 exposures of 1800 s each, for a total of 16 exposures (or 8 h of observation). We used the same fiber setup during all observing runs, and thus PNe and H II regions were observed within the same conditions, including the same exposure time. Priority was given to PNe when placing the fibers, since a set of H II region spectra already exists in the literature (GS87). A large number of fibers were devoted to sky measurements, to ensure that sky spectra were obtained in several positions around each target.

Cosmic rays were removed with the appropriate *hectospec.hcosmic* routine in the hectospec analysis package. Cosmic rays are detected via subtraction of multiple images, flagging the high or low pixels. The flagged pixels are interpolated over, and the resultant images are combined by average. This method avoids problems with clipping that other programs suffer from. In order to perform the sky subtraction we first inspected the sky spectra and eliminated those with unusual signals. Then we averaged the six spectra closer (in fiber location) to the targets, scaled the result to match the object spectrum, and subtracted.

The spectral calibration was achieved with the standard star Hilt600 (Massey et al. 1988), observed during the first night. This star was chosen by its excellent spectral coverage compared to the spectra of the PNe. It is worth noting that our analysis does not hinge on flux calibration, rather spectral calibration and flux ratios, thus this approach is sufficient to the science goals. Other stars were observed during the run nights, but the excellent spectral coverage of Hilt600 makes it the ideal choice for this type of calibration. Variations in sky conditions are taken into account since sky subtraction was performed before flux calibration.

In Table 1 we give the IDs, equatorial coordinates, and equivalent [O III] magnitude of the planetary nebulae and H II regions observed with MMT medium-resolution spectroscopy. All PN IDs are from Magrini et al. (2001), except for PN4 and PN5, which are identified PNe with unpublished positions (Magrini, private communication). There are 39 PNe and 20 H II regions whose spectra have been acquired and analyzed. With the exception of PN 49m and PN 79m, whose spectral lines are below the detection limit, we detect at least the major spectral lines in each target.

In Table 2, available online in its completeness, we give for each target the ion and wavelength (Cols. 1 and 2) of the observed emission line, then the relative observed flux (Col. 3), its uncertainty (Col. 4), and the line intensity (Col. 5) obtained with the extinction correction given as a header for each target. All fluxes and intensities are normalized for $F_{\mathrm{H}\beta} = 100$ and $I_{\mathrm{H}\beta} = 100$. Both PNe and H II regions are listed in Table 2. Target names are given for each target at the head of the corresponding flux list. The emission-line fluxes were measured with the package SPLOT of IRAF[1]. Errors in the fluxes were calculated taking into account the statistical error in the measurement of the fluxes, as well as systematic errors of the flux calibrations, background determination, and sky subtraction. Observations of same objects during different runs were stacked together and the resulting spectra have been used for the analysis.

We derived $c(\mathrm{H}\beta)$ from the Hα/Hβ flux ratios, as described in M09, and used the Galactic extinction curve by Mathis (1990) to correct the observed flux for interstellar extinction. In a few PNe the derived intensity of the Hγ line is more than 30% off the theoretical prediction ($I_{4340} = 0.466$ for $T_{\mathrm{e}} = 10\,000$ K, case B, Oserbrock & Ferland 2006). The reason for this offset could be an uncertain $c(\mathrm{H}\beta)$. The average $c(\mathrm{H}\beta)$ calculated for our PNe is 0.7 ± 0.3, a reasonable value if we consider the average $c(\mathrm{H}\beta)$ of Galactic PNe (from Cahn et al. 1992, $\langle c(\mathrm{H}\beta)\rangle = 0.95$) and the relative metallicities of the Galaxy to M 81. We will recall these outliers later in the discussion and indicate them with different symbols in the figures.

To our knowledge, this is the first attempt in the literature to detect PN emission line fluxes in M 81 thus we cannot extend our discussion to comparison with previous work. The spectral quality is excellent. In Fig. 1 we show a few examples of our M 81 PN spectra, where the plasma and abundance diagnostic lines are well evident, and the S/N obtained with our observations makes us confident on the data quality.

Several H II regions have been already observed by GS87, where the Authors refer to the catalog by Hodge & Kennicutt (1983) for coordinates. Since the latter are given in image coordinates rather than Galactic coordinates, it has been hard to eliminate from our sample of H II regions those that have been

[1] IRAF is distributed by the National Optical Astronomy Observatory, which is operated by the Association of Universities for Research in Astronomy (AURA) under cooperative agreement with the National Science Foundation.

Table 1. Observing log.

Id. (1)	α_{J2000} (2)	δ_{J2000} (3)	$m_{\lambda5007}$ (4)
PN 3m	9:54:26.54	69:10:30.5	24.41
PN 4	9:54:47.50	69:35:42.0	24.15
PN 4m	9:54:27.66	69:13:55.0	24.45
PN 5	9:54:53.80	69:08:01.0	23.87
PN 6m	9:54:36.70	69:17:00.5	24.39
PN 7m	9:54:38.52	69:10:36.8	24.53
PN 8m	9:54:45.50	69:08:06.6	24.06
PN 9m	9:54:46.52	69:05:39.0	23.66
PN 11m	9:54:53.15	69:13:32.2	24.51
PN 14m	9:54:09.28	69:11:31.0	24.75
PN 15m	9:55:01.01	69:12:04.3	24.45
PN 17m	9:55:10.09	69:02:37.1	24.24
PN 28m	9:55:13.62	69:07:10.3	23.91
PN 29m	9:55:14.78	68:55:30.0	23.56
PN 32m	9:55:15.70	69:08:39.8	24.23
PN 33m	9:55:15.96	69:13:31.7	24.30
PN 38m	9:55:19.47	68:54:45.7	24.39
PN 41m	9:55:02.58	69:06:26.3	23.77
PN 45m	9:55:21.81	69:07:50.6	23.86
PN 49m	9:55:23.38	69:02:50.9	23.66
PN 63m	9:55:28.25	69:01:26.5	24.26
PN 70m	9:55:30.62	69:07:56.3	23.66
PN 79m	9:55:34.58	69:09:00.9	24.49
PN 93m	9:55:39.07	69:05:42.1	23.48
PN 117m	9:55:50.11	68:59:48.4	24.04
PN 121m	9:55:51.46	69:05:14.9	23.56
PN 127m	9:55:52.93	69:10:52.1	24.60
PN 128m	9:55:53.02	69:06:15.2	24.19
PN 136m	9:55:06.11	68:57:18.5	24.60
PN 137m	9:55:07.29	69:12:10.4	24.47
PN 147m	9:56:20.74	68:58:26.8	24.41
PN 149m	9:56:27.09	69:05:26.4	23.66
PN 153m	9:56:28.70	69:00:32.8	23.56
PN 157m	9:56:31.99	69:03:31.3	24.09
PN 158m	9:56:32.84	69:03:58.8	24.23
PN 160m	9:56:04.48	69:06:36.0	24.31
PN 166m	9:56:08.41	69:08:37.8	24.49
PN 167m	9:56:08.54	69:03:56.0	24.53
PN 169m	9:56:09.87	68:59:56.0	24.39
H II 4	9:54:34.67	69:05:52.2	
H II 5	9:54:36.1	69:06:30.5	
H II 21	0:54:41.02	69:04:31.6	
H II 31	9:54:43.62	69:03:29.9	
H II 42	9:54:47.66	69:02:18.7	
H II 72	9:54:52.93	69:08:51.8	
H II 78	9:54:53.84	69:01:08.8	
H II 79	9:54:54.28	69:10:56.4	
H II 81	9:54:54.53	69:09:30.5	
H II 123	9:55:03.64	69:10:54.6	
H II 133	9:55:04.98	69:09:53.6	
H II 201	9:55:22.82	69:09:52.9	
H II 213	9:55:26.01	69:11:58.9	
H II 228	9:55:32.66	69:11:55.4	
H II 233	9:55:34.59	69:08:31.1	
H II 249	9:55:37.61	69:12:03.6	
H II 262	9:55:41.42	69:11:12.2	
H II 282	9:55:46.50	68:59:24.6	
H II 325	9:55:58.48	69:09:9.9	
H II 328	9:55:59.29	68:59:37.6	
H II 348	9:56:03.23	69:07:38.3	
H II 352	9:56:03.79	69:09:37.8	
H II 384	9:56:08.33	69:05:14.8	
H II 403	9:56:11.78	69:07:44	

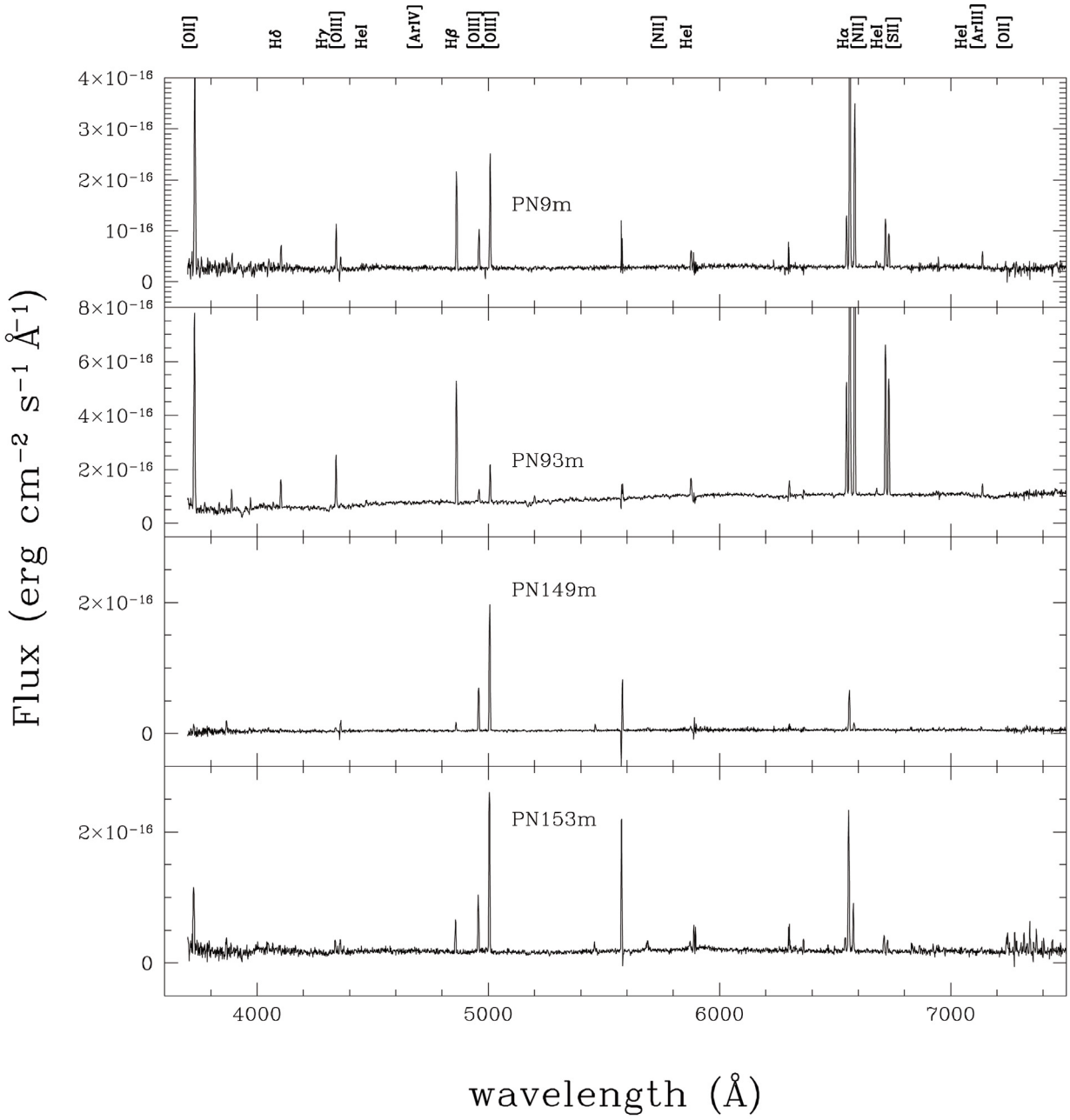

Fig. 1. Sample of medium-resolution spectra of M 81 PNe.

already analyzed by GS87 or comparing targets from the two sets. But by comparing the position visually, we did not find any obvious overlap between the two samples, thus cannot compare the results.

2.2. Plasma diagnostics

We perform plasma diagnostics by using the 5-level atom model included in the *nebular* analysis package in IRAF/STSDAS (Shaw & Dufour 1994), consistently with our work in M 33 (M09, M10). To calculate densities we use the doublet of the sulfur lines [S II]$\lambda\lambda$6716, 6731, while for the electron temperatures we use the ratios [O III]λ4363/(λ5007 + λ4959), [N II]λ5755/(λ6548 + λ6584), and [S III]λ6312/(λ9059 + λ9532). In some cases, even if the sulfur lines are available, their ratio is outside the diagnostic ranges for density calculation (e.g., Stanghellini & Kaler 1989), and we assumed a density of 10^3 cm^{-3}. We calculate the medium- and low-excitation temperatures respectively from the [O III] and [S III], and from the [N II] line ratios, respectively (see also Osterbrock & Ferland 2006, Sect. 5.2).

2.3. Abundance analysis

Of the 39 PNe with emission line spectra, [O III] and [N II] temperature diagnostics are available respectively for 10 and 12 PNe, with only 3 PNe in common. In the analysis of the M 33 PNe (M09) we were able to infer the electron temperature for targets whose plasma diagnostics were not available by using the correlation between the electron temperature and the He II line intensity. In the case of M 81 none of the PNe show the He II emission; as a consequence, abundance analysis was

Table 2. Observed fluxes and line intensities.

Ion	λ(Å)	F_λ	$\Delta(F_\lambda)$	I_λ
(1)	(2)	(3)	(4)	(5)
PN 3m, $c_\beta = 0.502 \pm 0.027$				
[O II]	3727	373.9	58.6	517.3
Hγ	4340	50.0	3.5	58.0
Hβ	4861	100.0	4.5	100.0
[O III]	4959	35.4	3.8	34.4
[O III]	5007	104.2	5.2	99.9
[N II]	5755	1.3	0.3	1.1
He I	5876	9.1	0.3	7.2
[N II]	6548	59.8	3.5	42.2
Hα	6563	412.0	6.9	290.1
[N II]	6584	142.5	4.5	100.0
[S II]	6717	60.3	3.8	41.4
[S II]	6731	44.3	3.4	30.4

Table 3. Plasma analysis and abundances.

(1)	(2)
Name	PN 3m
T_e[N II]	8893
N_e[S II]	100
He I/H	0.051
He/H	0.051
[O II]/H	3.320×10^{-4}
[O III]/H	5.440×10^{-5}
ICF(O)	1.0
O/H	3.864×10^{-4}
12 + log(O/H)	8.587
[N II]/H	2.916×10^{-5}
ICF(N)	1.164
N/H	3.394×10^{-5}
12 + log(N/H)	7.531
[S II]/H	2.250×10^{-6}
ICF(S)	1.001
S/H	7.066×10^{-6}
12 + log(S/H)	6.849

possible only for the 19 PNe where electron temperature was diagnosed directly. There are also 14 H II regions whose temperature analysis was based on auroral lines, and their plasma and abundance analysis was performed in a similar way than for the PNe. Electron temperature diagnostics for more than one excitation state was available for 5 of the 14 regions.

The plasma diagnostics are given in Table 3, available online, together with the ionic abundances of the PNe and H II regions. Column (1) gives the diagnostics, and Col. (2) the value as determined from our analysis. The targets are listed sequentially, as in Table 1, and the first line for each target gives the target name.

The abundance analysis of the PNe and the H II regions was performed following the prescription given by M09, M10; abundances of all elements except helium where calculated with the ionization correction factors (ICFs) given in Kingsburgh & Barlow (1994) for the case were only optical lines are detected. Where both T_e[O III] and T_e[N II] were available we used T_e[O III] to derive the abundances of medium and high excitation ions, and T_e[N II] for the low excitation ones. In several H II regions the temperature from the auroral line of [SIII] were also available, corresponding to transition of intermediate excitation. If only one of the electron temperature diagnostics was available we use that temperature to derive abundances for all ions. Helium abundances were calculated with the formulation of Benjamin et al. (1999) in two density regimes, and

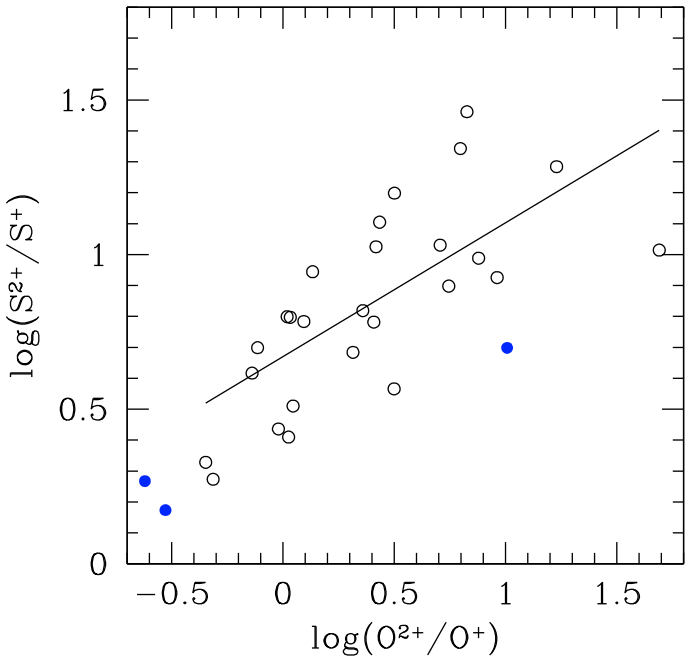

Fig. 2. The log(S^{2+}/log(S^+) versus log(O^{2+}/log(O^+) correlation (solid line), based on the Galactic PNe from Kingsburgh & Barlow (1994, open circles). Our targets are shown with filled circles.

Table 4. Temperatures and abundances uncertainties.

PN	ΔF_λ	ΔT_e[N II]	ΔT_e[O III]	ΔA(O)	ΔA(N)	ΔA(S)
	%	%	%	dex	dex	dex
(1)	(2)	(3)	(4)	(5)	(6)	(7)
PN 5	16	...	6	0.09	0.06	0.06
PN3m	23	8	...	0.17	0.11	0.10
PN9m	27,5	9	2	0.21	0.13	0.12
PN158m	48	...	23	0.29	0.20	0.19

taking into account Clegg's (1987) collisional populations, as in M09. The sulfur abundances for our PNe are mostly based on [S II] lines, thus highly unreliable. We used the interpolation to the Galactic PN data by Kingsburgh & Barlow to infer [S III]/[S II] from the [O III]/[O II] ratios, where possible, and obtained an estimate of [S III], which is observed only in three PNe. In order to check whether the sulfur correction is sensible, in Fig. 2 we plot log(S^{2+}/S^+) versus log(O^{2+}/O^+) for the Kingsburgh & Barlow sample. On the same plot we locate our M 81 PNe with measured [S III]. The solid line, representing $S^{2+}/S^+ = 4.677 \times \log(O^{2+}/O^+)^{0.433}$, has the correct slope for both the Galactic and M 81 data, but it overcorrect slightly for [S III]. Since the [S III] lines we observe in M 81 are quite faint, the relation by Kingsburgh & Barlow (1994) seems reasonable.

The formal errors in the ionic and total abundances were computed taking into account the uncertainties in (i) the observed fluxes; (ii) the electron temperatures and densities; and (iii) c(Hβ). We performed complete formal error propagation for a subsample of target, representing a spread of flux error and magnitudes, and realized that the errors in the electron temperature completely dominate the errors in the ionic abundances for all elements except helium. In particular, the flux uncertainty of the weaker of the diagnostic lines in the electron temperatures, λ5755 for T_e[N II] and λ4363 for T_e[O III], determine the errors in the abundances. In Table 4 we give the error analysis for the PN subsample, including the ones with the minimum and maximum flux errors; Col. (1) gives the PN name, Col. (2) gives the

Table 5. Galactocentric distances and elemental abundances.

Name	R_G [kpc]	He/H	A(N)	A(O)	A(Ne)	A(S)	A(Ar)
(1)	(2)	(3)	(4)	(5)	(6)	(7)	
PN 3m	10.49 ± 0.177	0.051 ± 0.002	7.53 ± 0.11	8.59 ± 0.17	...	6.85 ± 0.10	...
PN 5	6.276 ± 0.094	...	7.41 ± 0.06	8.17 ± 0.09	...	6.85 ± 0.06	6.37 ± 0.06
PN 9m	7.344 ± 0.156	0.101 ± 0.002	7.49 ± 0.13	8.54 ± 0.21	7.67 ± 0.12	6.51 ± 0.12	5.76 ± 0.12
PN 15m	9.006 ± 0.007	...	...	8.18 ± 0.16	...	...	...
PN 17m	4.858 ± 0.261	0.138 ± 0.015	7.59 ± 0.13	8.59 ± 0.21	...	6.87 ± 0.12	...
PN 29m	12.14 ± 0.415	0.109 ± 0.017	7.13 ± 0.05	8.24 ± 0.06	7.71 ± 0.05	6.41 ± 0.05	...
PN 33m	10.86 ± 0.110	...	7.07 ± 0.18	7.94 ± 0.28	...	6.43 ± 0.18	...
PN 38m	12.54 ± 0.385	0.122 ± 0.061	...	8.11 ± 0.22	...	...	6.08 ± 0.13
PN 41m	4.677 ± 0.110	0.179 ± 0.063	7.20 ± 0.18	8.11 ± 0.28	...	6.78 ± 0.18	...
PN 45m	4.326 ± 0.018	0.078 ± 0.006	7.84 ± 0.06	8.89 ± 0.09	...	6.95 ± 0.06	...
PN 63m	3.516 ± 0.117	0.089 ± 0.002	7.74 ± 0.14	8.62 ± 0.22	...	6.86 ± 0.13	...
PN 70m	4.785 ± 0.084	0.127 ± 0.005	7.67 ± 0.18	8.73 ± 0.28	...	6.97 ± 0.18	...
PN 93m	2.805 ± 0.109	0.068 ± 0.003	7.79 ± 0.05	8.51 ± 0.05	8.06 ± 0.05	7.10 ± 0.05	...
PN 121m	4.119 ± 0.218	0.184 ± 0.014	7.66 ± 0.3	8.81 ± 0.50	...	6.98 ± 0.30	...
PN 128m	5.339 ± 0.265	...	7.83 ± 0.18	8.27 ± 0.28	...	7.16 ± 0.18	...
PN 149m	10.14 ± 0.547	0.145 ± 0.018	7.60 ± 0.04	8.13 ± 0.04	7.62 ± 0.04	6.48 ± 0.04	5.84 ± 0.04
PN 153m	8.381 ± 0.277	0.147 ± 0.007	7.40 ± 0.13	8.31 ± 0.21	8.04 ± 0.12	6.78 ± 0.12	...
PN 157m	9.759 ± 0.493	0.201 ± 0.023	...	8.07 ± 0.04	...	...	...
PN 158m	10.15 ± 0.525	0.166 ± 0.078	7.37 ± 0.20	7.94 ± 0.29	7.40 ± 0.19	6.91 ± 0.19	...
Average		0.127 ± 0.045	$7.58^{+0.18}_{-0.30}$	$8.45^{+0.23}_{-0.54}$	$7.81^{+0.20}_{-0.38}$	$6.86^{+0.17}_{-0.28}$	$6.08^{+0.22}_{-0.48}$
H II 4	9.076 ± 0.396	0.079 ± 0.034	7.15 ± 0.33	8.58 ± 0.50	7.92 ± 0.34	6.45 ± 0.33	6.11 ± 0.33
H II 5	8.696 ± 0.342	0.072 ± 0.021	8.06 ± 0.07	8.87 ± 0.04	...	6.63 ± 0.03	5.87 ± 0.03
H II 31	8.648 ± 0.455	0.079 ± 0.026	7.60 ± 0.32	8.60 ± 0.50	...	6.87 ± 0.32	6.01 ± 0.32
H II 72	6.773 ± 0.070	0.086 ± 0.011	7.87 ± 0.13	8.82 ± 0.22	8.28 ± 0.13	6.79 ± 0.13	6.05 ± 0.13
H II 79	8.16 0 ± 0.006	0.077 ± 0.020	7.30 ± 0.29	8.26 ± 0.45	7.62 ± 0.29	6.63 ± 0.29	5.88 ± 0.29
H II 81	7.027 ± 0.031	0.104 ± 0.037	7.41 ± 0.32	8.40 ± 0.50	7.73 ± 0.32	6.59 ± 0.32	5.89±0.32
H II 123	7.762 ± 0.002	0.084 ± 0.007	7.40 ± 0.10	8.43 ± 0.18	7.68 ± 0.10	6.76 ± 0.10	6.30 ± 0.10
H II 133	6.721 ± 0.001	0.091 ± 0.159	7.90 ± 0.05	8.67 ± 0.04	8.19 ± 0.05	6.70 ± 0.05	6.04 ± 0.05
H II 201	6.750 ± 0.070	0.107 ± 0.032	7.63 ± 0.13	8.26 ± 0.22	7.73 ± 0.13	6.55 ± 0.13	5.97 ± 0.13
H II 228	9.849 ± 0.211	0.052 ± 0.021	7.41 ± 0.04	8.35 ± 0.04	...	6.79 ± 0.04	5.92 ± 0.04
H II 233	5.797 ± 0.138	0.086 ± 0.043	7.86 ± 0.25	8.50 ± 0.38	...	6.54 ± 0.25	...
H II 262	9.716 ± 0.280	0.073 ± 0.017	7.33 ± 0.07	8.32 ± 0.09	...	6.73 ± 0.07	6.06 ± 0.07
H II 325	9.261 ± 0.403	0.081 ± 0.042	7.23 ± 0.37	8.18 ± 0.60	...	6.42 ± 0.37	5.96 ± 0.37
H II 403	9.653 ± 0.493	0.069 ± 0.016	7.46 ± 0.13	8.57 ± 0.22	...	6.87 ± 0.13	6.21 ± 0.13
Average		0.082 ± 0.013	$7.63^{+0.23}_{-0.54}$	$8.54^{+0.18}_{-0.32}$	$7.95^{+0.22}_{-0.47}$	$6.69^{+0.12}_{-0.17}$	$6.04^{+0.13}_{-0.18}$

relative flux error for the weaker line in the temperature diagnostics (in PN 9m we could calculate both T_e[N II] and T_e[O III], thus we give the two errors), Cols. (3) and (4) give the relative errors in T_e[N II] and T_e[O III] respectively, and finally Cols. (5) through (7) give the abundance errors, in dex. We derived the errors for all other targets by interpolation of the $\Delta F_\lambda - \Delta A(X)$ curves. In the case of the helium abundances we run the error analysis by using the formulae by Benjamin et al. (1999), and found that the factor determining the uncertainties is the relative error on the helium flux lines. The abundances, their uncertainties, together with the galactocentric distances (see Sect. 3.1) are given in Table 5.

It is worth noting that another source of error that we could not estimate explicitly is intrinsic to the ICF method. The uncertainties due to the ICF are very moderate for oxygen, but can be quite large for the other atoms, especially sulfur, thus these abundance uncertainties should be considered as formal errors, but might underestimate the real uncertainties. Another source of abundance uncertainties is the use of a single electron temperature for both low- and high-ionization ions. This regards the 16 PNe and 9 H II regions where only one choice of the electron temperature was available. We have analyzed the sample of targets where two electron temperatures were available, and found that the average difference between electron temperatures of the order of 20%. We tested that the resulting atomic abundance uncertainties are lower than those due to flux errors on the auroral lines.

The sets where we have oxygen and neon in common is limited to 6 PNe and 7 H II regions. There is a clear correlation between these two α-elements in both sets, with correlation coefficients $R_{xy} = 0.7$ and 0.9 respectively for PNe and H II regions. This high correlation is expected, since both elements are produced in the type II SN environment. The large uncertainties in the sulfur abundances make the comparison between oxygen and sulfur less meaningful, although the two sets have higher overlap than the previously described pair (16 PNe and 14 H II regions in common), the correlation coefficient is only 0.4 and 0.3 for the two sets.

Figure 3 shows the log(N/O) vs. helium plot, to classify Type I PNe. These are the nitrogen and helium-enriched PNe, whose progenitors have likely undergo the third dredge-up and hot bottom-burning, and thus are likely to have higher progenitor masses (Peimbert & Torres-Peimbert 1983; Marigo 2001). The top right portion of the plot, where He/H > 0.125 and log(N/O) > −0.3, is the locus of type I PNe as determined for the Milky Way by Perinotto et al. (2004). Since the metallicity of M 81 is similar to that of the Milky Way, we can use the same diagnostic plot for M 81 PNe. Clearly, there are no type I PNe among those observed by us in M 81. In the next section we discuss the population of the observed PNe and its implications

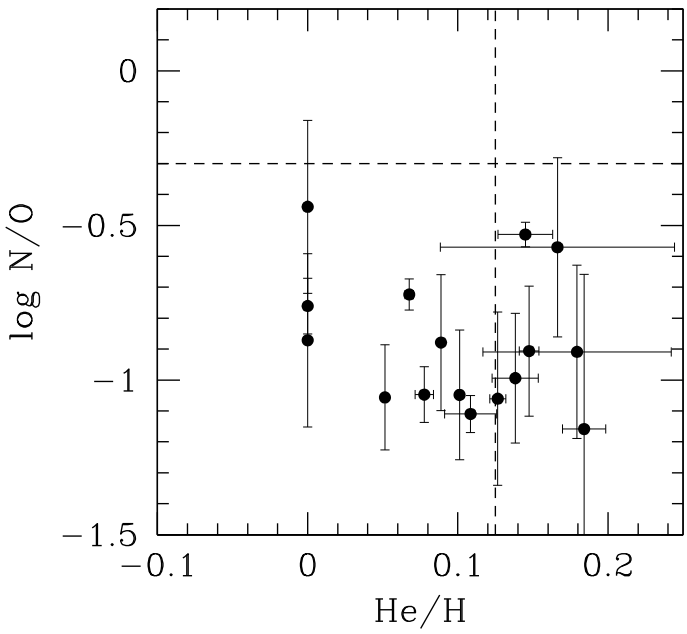

Fig. 3. log (N/O) vs. He/H; broken lines show He/H = .125 and log(N/O) = −0.3. Type I PNe would be located in the upper-right quadrant.

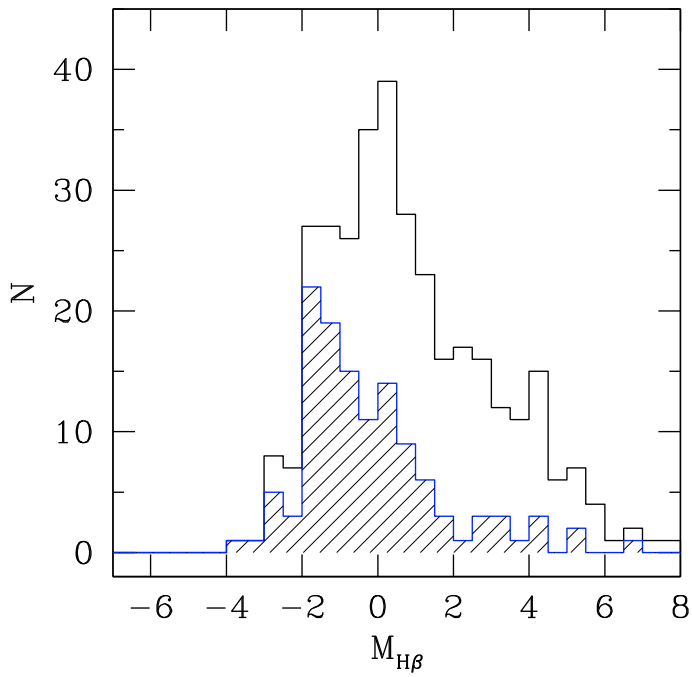

Fig. 4. The Galactic PNLF in the light of Hβ for a homogeneous sample of PN (unshaded histogram) and for a subsample of PNe with no He II emission lines (shaded histogram, see text). Data are from Cahn et al. (1992), Stanghellini & Haywood (2010).

for gradients and evolutionary studies, and show that indeed we do not expect an observed population of type I PNe among our targets.

In Table 5, at the bottom of each set of targets, we give the average abundances, relative to hydrogen (linear for helium, and in logarithmic format for the other elements. Uncertainties represent ranges of abundances). The average oxygen abundance of M 81 PNe ($2.83 \pm 2.01 \times 10^{-4}$) is lower that what has been inferred for the Galactic disk PNe ($4.49 \pm 2.28 \times 10^{-4}$ for type II PNe, Stanghellini & Haywood 2010) and about 1.6 higher than the average oxygen abundance of type II I PNe in M 33 (M09).

The H II regions observed by us span a small fraction of the galaxy radius (5.8 to 9.8 kpc from galaxy center). The average O/H value for these regions, $(3.42 \pm 1.78) \times 10^{-4}$, should be compared to the oxygen abundance of PNe in the same radial range, which is $(1.96 \pm 1.27) \times 10^{-4}$, showing a 0.25 dex oxygen enrichment in this area of the galaxy. The comparison between PNe and H II region average abundances of other elements is very limited, since the sets have 2 or 3 objects in common in the 5.8–9.8 kpc region.

2.4. The population of M 81 PNe

The PNe whose medium-resolution spectra are presented here are selected form the bright end of the planetary nebula luminosity function (PNLF) of the M 81 disk. They have two peculiarities, as a group: first, we do not detect the He II λ4686 emission lines in any of them; this is a signature of moderately low central star temperature (less than ~100 000 K). Second, none of the PNe whose abundance analysis was performed (i.e., whose electron temperature has been measured from the emission lines) is of type I, thus they must be the progeny of stars with turnoff masses ($M_{\rm to}$) in the ~1–2 $M_\odot$ range.

The properties of the M 81 PN sample are important to define their nature when we compare the population of M 81 PNe to those of other galaxies. M 81 has similar metallicity to that of the Milky Way (Davidge 2009). In M 81, as in most external galaxies, the observed PN population belong to the brightest few magnitude bins. The nature of the brightest PNe varies notably with the metallicity of the host galaxy. In their runaway evolution from the AGB, the PN central stars (CS) reach hot temperature while keeping very bright; later, both brightness and temperature decline. A PN is visible only when the CS temperature is high enough to ionize hydrogen, and the nebula is optically thin to the Hα radiation (e.g., Stanghellini & Renzini 2000). At relatively high metallicities such as those of M 81 or the Galaxy, the brightest PNe are not those with the hottest CSs (e.g., Villaver et al. 2002). In fact, the post-AGB shells with very hot CSs are statistically still enshrouded in dust at early phases or their evolution, thus still thick to the Hα radiation. A lower metallicity implies a shorter thinning time (Käufl et al. 1993). Plenty of type I PNe have been observed within the bright end of the PNLF of low metallicity galaxies such as M 33, the LMC, and the SMC; this is not the case in M 81, where the high metallicity prevents massive progenitor PNe (i.e., the type I) to populate the bright end of the PNLF.

To illustrate this point, in Fig. 4 we show the luminosity function (PNLF) of Galactic PNe in the Hβ-equivalent absolute magnitude. The Hβ fluxes are from Cahn et al. (1992), and the PN distances from Stanghellini et al. (2008; see also Stanghellini & Haywood 2010). The solid histogram represents the homogeneous Galactic sample of 331 PNe where both distance and Hβ flux are known, and where spectroscopy has been performed and a lower limit or a detection of the He II λ4686 line has been acquired. The shaded histogram is the subsample of Galactic PNe with $I_{4686}/I_\beta < 5\%$. It is clear that at least 80–90% of the bright Galactic PNe do not show the He II lines, in qualitative agreement with not finding this emission line in the M 81 PN sample.

In order to quantify the expectation of detecting the He II emission line in a given PN population of a certain metallicity we use Käufl et al.'s (1993) models to derive PN opacity, where the non-evolving term of the opacity,$\tau_\lambda(0)$, scales

Table 6. Metallicity gradients.

X	$N_{\rm PNe}$	$\Delta\log(X/H)/\Delta R_G$	$A(X)_0$
(1)	(2)	(3)	(4)
O	19	-0.055 ± 0.02	8.72 ± 0.18
Ne	6	-0.047 ± 0.03	8.18 ± 0.27
S	16	-0.069 ± 0.01	7.27 ± 0.10
X	$N_{\rm H\,II\ reg.}$	$\Delta\log(X/H)/\Delta R_G$	$A(X)_0$
O	31	-0.093 ± 0.02	9.37 ± 0.24

directly with the dust-to-gas ratio (see their Eq. (10)). We also express this ratio as expected at different metallicities, $M_{\rm d}/M_{\rm g} \sim 0.01({\rm O/H})/({\rm O/H})_{\rm MW}$ (Draine 2009), where the right hand side term refers to the ratio of the oxygen vs. hydrogen abundance in a given galaxy compared to that of the Milky Way. To obtain the ratio for M 81 scaled to that of the Galaxy we use the H II region oxygen abundances in M 81 (4.99×10^{-4}) and in the Galaxy (5.25×10^{-4}, Deharveng et al. 2000) to find $M_{\rm d}/M_{\rm g} \sim 0.01$, thus for a given type of M 81 PN the thinning time would be similar to that of the Galactic homologous. We conclude that the lack of He II-emitting PNe in M 81 is totally expected, given the Galactic PNLF for both He II-emitting and non-emitting PNe (Fig. 4).

It is interesting to compare the PN population of M 81 with that of M 33 as well. Magrini et al. (2010) obtained an average oxygen abundance of $\langle {\rm O/H}\rangle = 2.04\times10^{-4}$ for H II regions in the M 33 disk, corresponding to a dust-to-mass ratio of $\sim 4\times10^{-3}$, or, less than half that of M 81. By running the Käufl et al.'s models for M 33 we obtain (Balmer line) thinning times ~1.5 times shorter than in M 81 or the Galaxy, which can account for the relatively higher frequency of He II-emitting, bright PNe that where observed in M 33 by M09.

We know that the brightest PNe in a given population excludes the progeny of the massive AGB stars, i.e., those with $M_{\rm to} > 2\ M_\odot$ (Stanghellini & Renzini 2000). The sample of M 81 PNe under study here thus does not include the progeny of the more massive AGB stars. This agrees very well with the observational fact that we do not observe any type I PNe in our M 81 sample.

3. Radial metallicity gradients in M 81

3.1. The planetary nebula gradients

The metallicity gradient of a disk galaxy is generally intended as the metallicity variation between the galactic center and the periphery, measured radially. These gradients are essential constraints for the chemical evolution models, and, depending on the probe, can constrain the galactic composition at different times in evolution. Planetary nebulae with low-mass progenitors, such as non-type I PNe, probe the early stages of disk metallicity. We could derive the metallicity gradients in M 81 from oxygen abundances, thus probing the α-element evolution through the galactic disk. We estimate the distances of our target PNe from the center of M 81 by using a rotation angle of 157° and an inclination of 59°. The error in the target coordinates is very low, and the major source of error in the distance calculation is the uncertainty in the galaxy inclination, which we take as in Connolly et al. (1972), ±2°, and we propagate to estimate the galactocentric distance uncertainties.

In Table 6, Cols. (3) and (4), we give the metallicity gradients calculated for oxygen, neon, and sulfur. Slopes are in dex kpc^{-1}, while intercepts are in dex, with the usual notation

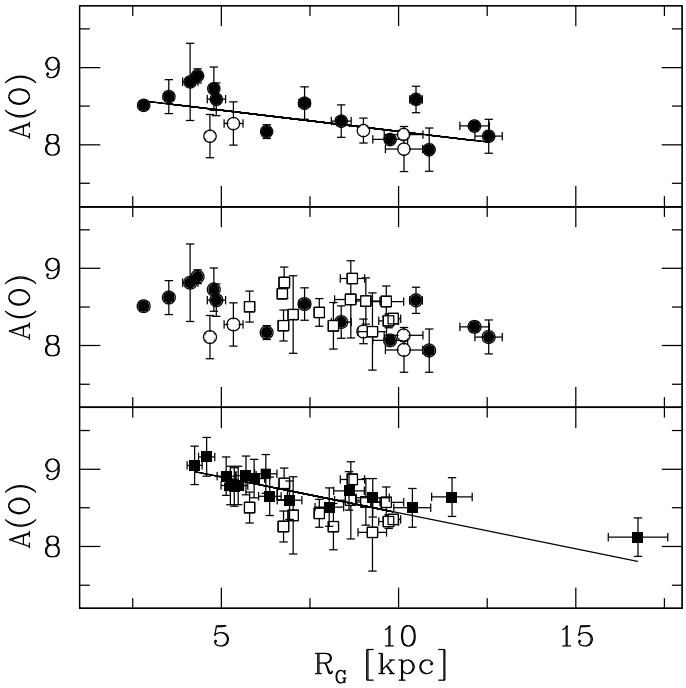

Fig. 5. Oxygen abundances vs. galactocentric distances for M 81 targets. *Top panel*: the observed sample of PNe, with formal error bars and least square fit represented by solid line. Open symbols represent those PNe whose extinction constant might be overestimated. *Middle panel*: the H II region sample from MMT spectra (open squares) superimposed to the PN population of the top panel. *Bottom panel*: the H II regions from GS87 (filled squares) superimposed to the MMT H II regions of the middle panel (open squares). The line represents the least square fit for the combined sample, as given in Table 6.

of $A({\rm X}) = \log({\rm X/H}) + 12$. In Fig. 5 (top panel) we show the oxygen gradient from the M 81 PNe, where the line represent the linear fit. Only PNe are plotted in this top panel, with filled symbols representing the general PN population, and the open symbols indicating those PNe whose extinction correction from the Hα/Hβ ratio does not well reproduce the line intensity expected for the Hγ emission line. These open data points might thus have larger uncertainties than inferred from the formal error analysis.

We perform the fits with the routine *fitexy* (see Numerical Recipes, Press et al. 1992) and obtain $\Delta\log({\rm O/H})/\Delta R_{\rm G} = -0.055 \pm 0.02$ dex kpc^{-1}. Should we exclude the open symbols in the fit we would obtain a very similar result ($\Delta\log({\rm O/H})/\Delta R_{\rm G} = -0.053 \pm 0.02$ dex kpc^{-1}).

In Fig. 6 we show the metallicity gradients for sulfur (top) and neon (bottom), where the PNe are plotted with filled symbols. The solid lines represent the fits obtained with the *fitexy* routines that consider the formal errors both in abundances and distances (see Table 6). Fits obtained with the least square method are very similar.

3.2. H II regions in the A(X)–$R_{\rm G}$ plots

The bottom panel of Fig. 5 shows the H II region analysis of oxygen abundances from this paper (open symbols) and from GS87 (filled symbols). Formal errorbars have been applied to the data obtained in this paper, while in the case of the GS87 sample we assume a 0.05% relative uncertainty in the distances, and a 0.25 dex uncertainty in the oxygen abundances. It is worth noting that we have recalculated the galactocentric distances for the GS87 targets by assuming the same distance to M 81 than

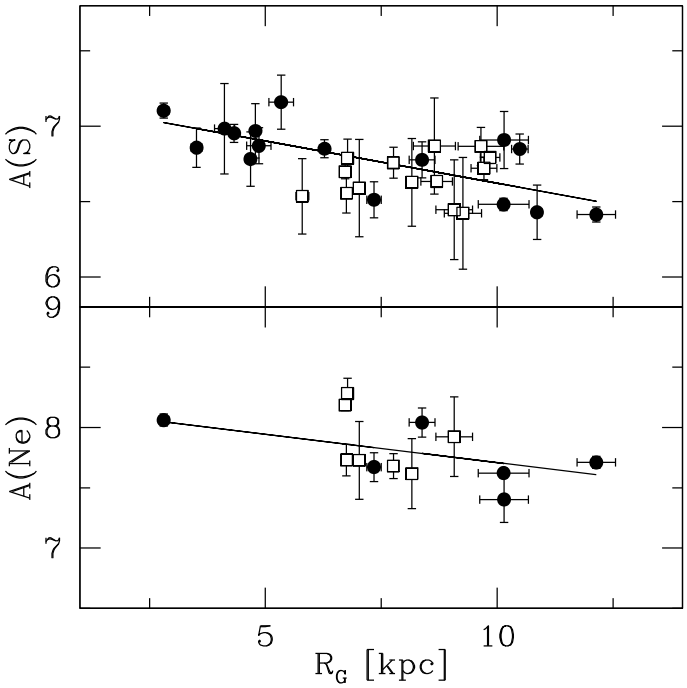

Fig. 6. Sulfur (*top panel*) and neon (*bottom panel*) abundances from MMT observations vs. galactocentric distances for M 81 PNe (filled circles) and H II regions (open squares). The lines represent the linear fits to the PNe as discussed in the text.

we use thorough this paper (d = 3.63 Mpc) for homogeneity, although this does not affect the resulting gradient significantly. The composite data sample has been fitted including the distance and abundances uncertainties with the *fitexy* routine, to give a gradient ($\Delta\log(\mathrm{O/H})/\Delta R_{\mathrm{G}} = -0.093 \pm 0.02$ dex kpc^{-1}) not too dissimilar, yet steeper, from that of PNe. A direct least square fit would give a slightly milder gradient ($\Delta\log(\mathrm{O/H})/\Delta R_{\mathrm{G}} = -0.07$ dex kpc^{-1}). It is worth noting that both the average O/H abundance in H II regions and the intercept of the linear metallicity gradient are consistently higher that the respective values for PNe, as shown in Table 6, with PNe under abundant with respect to H II regions by almost a factor of 2, on average. This is well seen in the middle panel of Fig. 5, where PNe and H II regions from MMT observations are plotted together.

In Fig. 6 we show the sulfur (top) and neon (bottom) abundances in H II regions versus their galactocentric distances (open symbols), plotted together with the PN data (filled symbols). Since the H II regions observed with the MMT span a small fraction of the galaxy radius, metallicity gradients derived form these species would not be very meaningful. Within the distance ranges populated by our H II region data we find $\langle\mathrm{Ne/H}\rangle_{\mathrm{H\,ii}}/\langle\mathrm{Ne/H}\rangle_{\mathrm{PN}} = 1.1$, and $\langle\mathrm{S/H}\rangle_{\mathrm{H\,ii}}/\langle\mathrm{S/H}\rangle_{\mathrm{PN}} = 0.9$. Any further comparison is not sensible given the limited data at hand, and we prefer to postpone a complete discussion of the sulfur and neon abundances in PNe as compared to the H II regions of M 81 when more H II region spectral data with diagnostic lines relative to these atoms will be available.

4. Discussion

4.1. Galaxy evolution through oxygen abundances

The O/H abundances are among the most reliable in emission-line targets when only optical spectra are available. In the case of M 81, PNe and H II regions provide a meaningful comparison between young and old stellar objects, since the techniques of data acquisition, analysis, and abundance calculation are the same for both classes of objects. In particular, for several H II regions presented here, those observed with the MMT, the actual data acquisition is identical that that of the PNe, thus the comparison among data set is even more compelling.

It is worth emphasizing that the H II region gradient is not based exclusively on our MMT data, which cover a limited radial range, but also on the results by GS87. The spectroscopic observations of GS87 did not allow a direct measurement of the electron temperature. They derived T_{e} by applying an indirect calibration made through the photoionization models by Pagel et al. (1979). The errors on the electron temperature are estimated of the order of ±1200 K, mainly due to the scatter of the measurements on which Pagel et al. (1979) based their calibrations. We have estimated, using the IRAF *ionic* task, that an uncertainty of ±1200 K in T_{e} translates in ±0.2 dex in the ionic abundances. Thus, the chemical abundances of GS87 result less accurate than ours, and may introduce biases in the determination of the gradient. We conservatively have assumed uncertainties of 0.25 dex for the oxygen abundances from GS87.

As shown in Fig. 5, the radial oxygen gradient slope of H II regions is mildly steeper than that of PNe, with differences compatible with the slope uncertainties. Since there are no type I PNe in our sample it is sensible to assume that the PN progenitor (turnoff) masses are smaller than ~2 $M_{\odot}$, implying a population older than t ~1 Gyr (Maraston 1998). The lower limit for PN progenitor mass is around 1 $M_{\odot}$, corresponding to a galactic age of t ~10 Gyr.

In Fig. 7 we plot the slope of the oxygen radial gradients in M 81 (squares) for PNe and H II regions, against the mean age of the population considered. H II regions are placed at $t = 0$, while PN ages are inferred from the presumed mass of progenitors (see Stanghellini & Haywood 2010, for a detailed discussion of the different PN types). The horizontal error bar for PNe indicates the age range of the population, while all vertical error bars indicate the uncertainties in the slopes. It appears that the slope of the M 81 metallicity gradient did not vary very much during the past 10 Gyr. A flattening with time, as predicted by many chemical evolution models, is not supported by our observations. On the contrary, a constant slope, or a mild steepening of gradient slopes with time is inferred.

While uncertainties in the actual slopes are high, it is worth comparing the results of M 81 with what found in M 33 PNe and H II regions (M09 and M10, starred symbols), and the Milky Way (PNe from Stanghellini & Haywood 2010; H II regions from Deharveng et al. 2000, filled circles). The metallicity gradients are generally steeper in M 81 than in either the Milky Way and M 33, but in all three galaxies we observe mild flattening with the age of the population, going from steeper for H II regions to flatter for non-type I PNe. It is worth noting that in the Galaxy the PN types I, II, and III were independently selected to calculate the oxygen radial gradients, while in M 33 we were able to distinguish between type I and non-type I.

Since the gradient slopes seem to flatten with the age of the population considered, there is an indication that the gradients themselves are steepening with the galaxy age in all the three galaxies considered. It is a mild steepening, and with large uncertainties, but it is consistently found in all three galaxies, so it is worth exploring it.

Let us recall that the slope of the H II gradient in M 33 excluded the central kpc, as explained by M 10. If we were including H II regions in the central kpc we would obtain nearly no gradient evolution between H II regions and type I PNe in M 33.

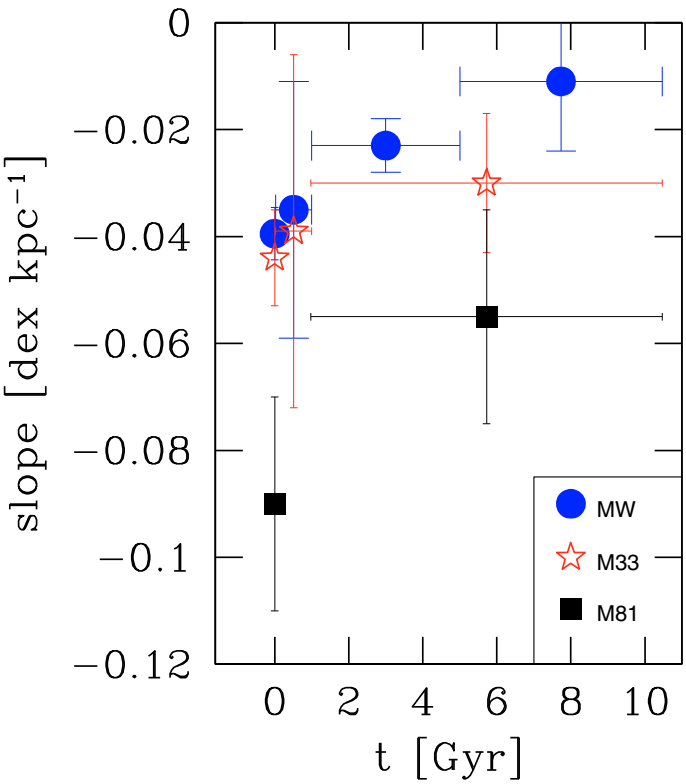

Fig. 7. The slope of the oxygen gradients, in dex kpc^{-1}, versus the age of the stellar population considered, for the Galaxy (filled circles, adapted from Stanghellini & Haywood 2010), M 33 (starred symbols, adapted from M09 and M10) and M 81 (squares, this paper). The zero-age populations represent the slopes of the gradients estimated though H II region oxygen abundances, while all other points are slopes of PN gradients, see text. Error-bars in the x direction represent the approximate age span of the populations, and in the y direction are the estimated metallicity uncertainties. The zero-age data point for M 81 is uncertain, as it is based on the combination of of the H II regions observed with the MMT and the GS87 sample.

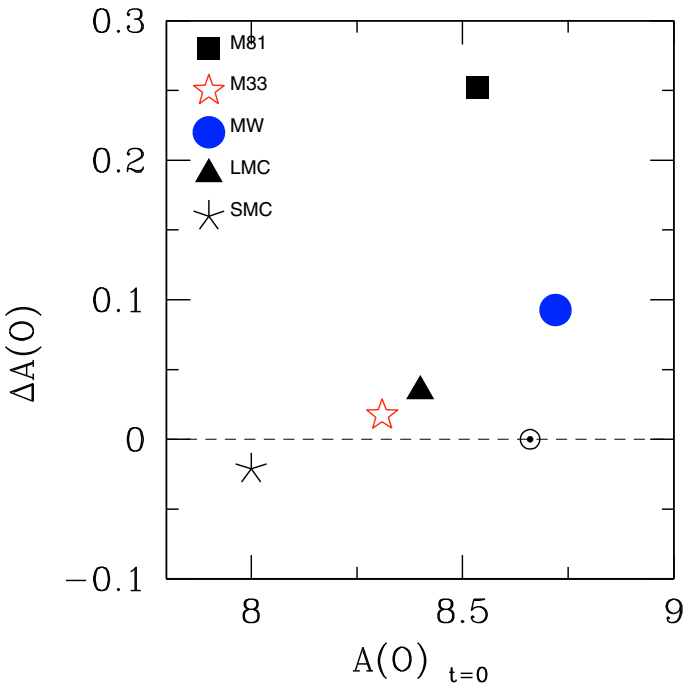

Fig. 8. Difference between average oxygen abundance of H II regions and non-type I PNe vs. zero-age average oxygen abundance for M 81 (square, this paper), compared to that of M 33 (starred symbol, M09 and M10), the Magellanic Clouds (LMC: triangle, SMC: diamond; Garnett 1999; M09), and the Milky Way (filled circle, Stanghellini & Haywood 2010; Peimbert 1999). The solar value represented is from Asplund et al. (2005). The M 81 datum is derived from PN and H II regions in the 5.8–9.8 kpc range, and does not include the GS87 data. The M 81 galaxy shows considerable metal enrichment.

There is thus some evolution of the oxygen gradients with time, where the slopes vary by 1×10^{-2} to $\sim3\times10^{-3}$ dex per radial kpc in ~10 Gyr. Stanghellini & Haywood (2010) offer the hypothesis that portions of the Milky Way at different radial distances might have evolved at different rates. The model by Schönrich & Binney (2009) illustrates this type of evolution, which could hold as well for the other spiral galaxies and for M 81.

In Fig. 8 we show the global oxygen evolution in different galaxies, where average oxygen abundances in H II regions are plotted against the same quantities in non-type I PNe. In the case of the disk galaxies, both populations cover a reasonable radial range and are representative of the whole disks. The SMC and LMC oxygen abundance are from Leisy & Dennefeld (2006), and the H II regions in the Magellanic Clouds are from Dennefeld (1989). The samples of PNe and H II regions considered in the Galaxy and M 33 are as described earlier in this section. M 81 PN and H II regions abundances are from this paper, both selected consistently within the galactocentric distance domain where both sets of targets coexist. The solar point is from Asplund et al. (2005). In this plot M 81 stands out as the galaxy with most chemical enrichment in the group considered. M 33, as found by M10, shows almost no enrichment, and the other galaxies show either low enrichment (the Galaxy and the LMC) or slight depletion of oxygen in the SMC, where the cause could be extremely efficient ON cycle at very low metallicity (Karakas & Lattanzio 2007). The average enrichment of M 81 is 0.25 dex.

The M 81 galaxy disk shows indication of chemical enrichment through oxygen abundances. It also shows generally steeper metallicity gradients than both M 33 and the Galaxy. The non-type I PNe gradients in M 81 is −0.055 dex kpc^{-1}, while homologous slopes are −0.03 and −0.02 dex kpc^{-1} respectively in M 33 and the Galaxy, indicating that whatever process produces the metallicity gradients in spiral galaxies, it is more efficient in M 81 and the overall galaxy metallicity is not a factor. Similarly for H II regions, the M 81 gradient slope is −0.09 dex kpc^{-1}, to be compared with −0.044 and −0.04 dex kpc^{-1} for M 33 and the Milky Way respectively. Indication of steeper gradients, and sizable chemical evolution, are thus the defining characteristics of M 81 compared with other spirals. The oxygen enrichment indicates that this galaxy has suffered outflow to a lesser extent than the comparison galaxies, and steeper oxygen gradients are compatible with this explanation.

4.2. *The chemical evolution of M 81: comparison with the Milky Way*

It is evident from the above analysis that the metallicity gradient slopes in the galaxies examined do not depend on the average galactic metallicity: M 33 is metal poor (its metallicity is similar to that of the LMC, Leisy & Dennefeld 2006) and M 81 is closer in metal contents to the Galaxy. Since M 81 is also closer to the Galaxy in stellar mass content (see Table 7 for a direct comparison of the main properties of these two galaxies), it makes sense to compare these two galaxies directly, to explore the relations of

Table 7. Properties of M 81 and the Galaxy.

	M 81	MW
Morphological type	Sa	Sbc
Total mass [$M_\odot$]	2.3×10^{11}(a)	$1.8–3.7 \times 10^{11}$ (b)
Gas mass [$M_\odot$]	2.9×10^{9}(c)	4×10^{9} (d)
Luminosity [$L_\odot$]	1.9×10^{10} (a)	...
Total SFR [$M_\odot$ yr^{-1}]	0.4–0.8 (e)	0.35 (f)
Max $V_{\rm rot}$ [km s^{-1}]	260 (g)	200 (h)

Notes. (a) Appleton et al. (1981); (b) Hodge & Miller (1992); (c) Karachentsev & Kashibadze (2006); (d) van der Kruit (1990); (e) Gordon et al. (2004); (f) Walterbos & Braun (1994); (g) Rohlfs & Krertschmann (1980); (h) MD05.

the metallicity gradients to the characteristics of the galaxy disks and to their evolution. The observations of PNe tell us that the gradient of M 81 is steeper than that of our Galaxy in old stellar populations; the trend seems to persist in the young stellar population, but this needs further confirmation.

From a theoretical point of view, there are two main reasons that could influence the gradient slopes, (1) the rotational velocity of the galaxy and (2) the different situation of these two galaxies within their environment.

Mollá & Diaz (2005) noted that metallicity gradients depend on the rotational velocity of the galaxy (thus presumably on its total mass), and on its morphological type: more massive galaxies tend to evolve faster and have flatter gradients than lower mass galaxies; for a given rotation velocity, gradients are steeper for late type than for early type galaxies. Both effects would imply a steeper gradient for the Galaxy than for M 81, contrary to the observations. Some other factor must be at play.

It is likely that the situation of M 81 within its group of galaxies influences its metallicity gradient. The tidal H I features near M 81 are consistent with a large-scale redistribution of gas in this galaxy. M 81 is the only massive galaxy of its group, surrounded by several small galaxies. The interaction of M 81 with the dwarf galaxies of its group probably steepens the gradient of the major member due to the effect of stripping gas from the external regions of the major companion, while interaction of galaxies with more or less the same mass would redistribute the gas in both galaxies, and thus flatten the gradient.

The chemical evolution models of Valle et al. (2005) consider the effects of gas stripping due to galaxy encounters on the star formation rate and the evolution of the metallicity. They found that, for a stripping occurring 1–3 Gyr after the formation of the galaxy and removing 97% of the gas, the region affected by the gas removal has a SFR almost a factor of 10 lower than in the model without stripping and the relative metallicity is then reduced by about 40%. The metallicity reduction is not strongly dependent on the time and duration of the stripping episode, but is quite sensitive to the relative amount of gas removed from the region. This effect should be more pronounced in the outer than the inner galactic regions, due to the proximity of the interacting galaxies, and it might explain why M 81 has steeper metallicity gradients than the Galaxy. Unfortunately, the models by Valle et al. (2005) are limited to a single radial region, thus this conclusion is of qualitative nature. A radially-resolved chemical evolution modeling taking into account the effects of stripping would be necessary to determine the effect of tidal interaction on the gradient, and also to compare with other results.

5. Conclusions

Hectospec/MMT spectroscopy of a sizable sample of PN and H II regions in the nearby M 81 galaxy has proven very efficient to find chemistry of the young and old stellar populations, and to pin point the radial metallicity gradients. We were able to detect the diagnostic lines for plasma and abundance analysis in 19 PNe and 14 H II regions. Their analysis indicates that the galaxy is clearly chemically enriched, with $\langle$O/H$\rangle_{\rm H\ ii\ reg.}/\langle$O/H$\rangle_{\rm PN}$ = 1.8, from MMT spectra where PNe and H II regions were simultaneously acquired. We also found that there is a noticeable PN metallicity gradient in oxygen, with Δlog(O/H)/$\Delta R_{\rm G}$ = −0.055 dex kpc^{-1}, and that neon and sulfur gradient slopes are within 15% of the oxygen one. The MMT sample of H II regions have limited galactocentric distribution, thus they are insufficient probes of the metallicity gradient. The gradient slope from the combined MMT and GS87 H II region samples is steeper (−0.093 dex kpc^{-1}) than that of the PNe, possibly indicating an evolution of the radial metallicity gradients with time: older stellar population show shallower gradients, thus gradients are steepening with the time since galaxy formation. These results have been compared to their homologous for the Milky Way and M 33, where similar (yet less marked) gradient steepening is inferred. We plan to increase the size of the H II region sample, and to extend their gradient study to other atoms such as neon and sulfur in the near future, for a more complete comparison with the PNe, with the goal of obtaining firmer observational constraints for the chemical evolutionary models.

Acknowledgements. The observations reported here were obtained at the MMT Observatory, a facility operated jointly by the Smithsonian Institution and the University of Arizona. MMT telescope time was granted by NOAO, through the Telescope System Instrumentation Program (TSIP). TSIP is funded by NSF. We warmly thank D. Fabricant for making Hectospec available to the community, and the Hectospec instrument team and MMT staff for their expert help in preparing and carrying out the Hectospec observing runs. We thank N. Caldwell, D. Ming, and their team for the help during the data reduction. L.S. acknowledges the *Observatoire de Paris* and the *Osservatorio Astrofisico di Arcetri* for their hospitality during different stages of this project.

References

Appleton, P. N., Davies, R. D., & Stephenson, R. J. 1981, MNRAS, 195, 327
Asplund, M., Grevesse, N., & Sauval, A. J. 2005, Cosmic Abundances as Records of Stellar Evolution and Nucleosynthesis, 336, 25
Benjamin, R. A., Skillman, E. D., & Smits, D. P. 1999, ApJ, 514, 307
Cahn, J. H., Kaler, J. B., & Stanghellini, L. 1992, A&AS, 94, 399
Clegg, R. E. S. 1987, MNRAS, 229, 31
Connolly, L. P., Mantarakis, P. Z., & Thompson, L. A. 1972, PASP, 84, 61
Davidge, T. J. 2009, ApJ, 697, 1439
Deharveng, L., Pena, M., Caplan, J., & Costero, R. 2000, MNRAS, 311, 329
Dennefeld, M. 1989, Recent Developments of Magellanic Cloud Research, 107
Dors, O. L., Jr., & Copetti, M. V. F. 2006, A&A, 452, 473
Draine, B. T. 2009, EAS Publications Series, 35, 245
Fabricant, D., Fata, R., Roll, J., et al. 2005, PASP, 117, 1411
Freedman, W. L., Madore, B. F., Gibson, B. K., et al. 2001, ApJ, 553, 47
Garnett, D. R. 1999, New Views of the Magellanic Clouds, 190, 266
Garnett, D. R., & Shields, G. A. 1987, ApJ, 317, 82 (GS87)
Gordon, K. D., Pérez-González, P. G., Misselt, K. A., et al. 2004, ApJS, 154, 215
Gottesman, S. T., & Weliachew, L. 1975, ApJ, 195, 23
Henry, R. B. C., Kwitter, K. B., & Balick, B. 2004, AJ, 127, 2284
Hodge, P., & Miller, B. 1992, BAAS, 24, 1201
Hodge, P. W., & Kennicutt, R. C., Jr. 1983, AJ, 88, 296
Jacoby, G. H., Ciardullo, R., Booth, J., & Ford, H. C. 1989, ApJ, 344, 704
Käufl, H. U., Renzini, A., & Stanghellini, L. 1993, ApJ, 410, 251
Karakas, A., & Lattanzio, J. C. 2007, Publications of the Astronomical Society of Australia, 24, 103
Karachentsev, I. D., & Kashibadze, O. G. 2006, Astrophysics, 49, 3
Kingsburgh, R. L., & Barlow, M. J. 1994, MNRAS, 271, 257
Kong, X., Zhou, X., Chen, J., et al. 2000, AJ, 119, 2745
Leisy, P., & Dennefeld, M. 2006, A&A, 456, 451

Lin, W., Zhou, X., Burstein, D., et al. 2003, AJ, 126, 1286
Maciel, W. J., & Quireza, C. 1999, A&A, 345, 629
Magrini, L., Perinotto, M., Corradi, R. L. M., & Mampaso, A. 2001, A&A, 379, 90
Magrini, L., Corbelli, E., & Galli, D. 2007, A&A, 470, 843
Magrini, L., Stanghellini, L., & Villaver, E. 2009, ApJ, 696, 729 (M09)
Magrini, L., Stanghellini, L., Corbelli, E., Galli, D., & Villaver, E. 2010, A&A, 512, A63 (M10)
Marigo, P. 2001, A&A, 370, 194
Massey, P., Strobel, K., Barnes, J. V., & Anderson, E. 1988, ApJ, 328, 315
Mathis, J. S. 1990, ARA&A, 28, 37
Maraston, C. 1998, MNRAS, 300, 872
Mollá, M., & Díaz, A. I. 2005, MNRAS, 358, 521 (MD05)
Osterbrock, D. E., & Ferland, G. J. 2006, Astrophysics of gaseous nebulae and active galactic nuclei, 2nd. edn., ed. D.E. Osterbrock, & G.J. Ferland (Sausalito, CA: University Science Books)
Pagel, B. E. J., Edmunds, M. G., Blackwell, D. E., Chun, M. S., & Smith, G. 1979, MNRAS, 189, 95
Peimbert, M. 1999, Chemical Evolution from Zero to High Redshift, 30
Peimbert, M., & Torres-Peimbert, S. 1983, in Proc. Symp. (Dordrecht: D. Reidel Publishing Co.), 233
Perinotto, M., & Morbidelli, L. 2006, MNRAS, 372, 45
Perinotto, M., Morbidelli, L., & Scatarzi, A. 2004, MNRAS, 349, 793
Press, W. H., Teukolsky, S. A., Vetterling, W. T., & Flannery, B. P. 1992, (Cambridge: University Press), 2nd edn.
Rohlfs, K., & Kreitschmann, J. 1980, A&A, 87, 175
Sabbi, E., Gallagher, J. S., Smith, L. J., de Mello, D. F., & Mountain, M. 2008, ApJL, 676, L113
Shaw, R. A., & Dufour, R. J. 1994, ASPC, 61, 327
Schönrich, R., & Binney, J. 2009, MNRAS, 396, 203
Stanghellini, L., & Kaler, J. B. 1989, ApJ, 343, 811
Stanghellini, L., & Renzini, A. 2000, ApJ, 542, 308
Stanghellini, L., & Haywood, M. 2010, ApJ, 714, 1096
Stanghellini, L., Guerrero, M. A., Cunha, K., Manchado, A., & Villaver, E. 2006, ApJ, 651, 898
Stanghellini, L., Shaw, R. A., & Villaver, E. 2008, ApJ, 689, 194
Valle, G., Shore, S. N., & Galli, D. 2005, A&A, 435, 551
van der Kruit, P. C. 1990, The Milky Way as a Galaxy, 331
Walterbos, R. A. M., & Braun, R. 1994, ApJ, 431, 156
Villaver, E., Manchado, A., & García-Segura, G. 2002, ApJ, 581, 1204
Weisz, D. R., Skillman, E. D., Cannon, J. M., et al. 2008, ApJ, 689, 160
Yun, M. S., Ho, P. T. P., & Lo, K. Y. 1994, Nature, 372, 530
Yun, M. S. 1999, Galaxy Interactions at Low and High Redshift, 186, 81
Zaritsky, D., Kennicutt, R. C., Jr., & Huchra, J. P. 1994, ApJ, 420, 87